

# A method based on an artificial neural network for discriminating Compton scattering events in a high-purity germanium $\gamma$ -ray spectrometer

Chun-Di Fan, Guo-Qiang Zeng\*, Hao-Wen Deng, Lei Yan, Jian Yang, Chuan-Hao Hu, Song Qing, Yang Hou

College of Nuclear Technology and Automation Engineering, Chengdu University of Technology, Chengdu, China

\*Corresponding author. E-mail address: [zgq@cdut.edu.cn](mailto:zgq@cdut.edu.cn). Tel.: +1388 193 6804.

**Abstract:** To detect radioactive substances with a low activity level, an anti-coincidence detector and high-purity germanium detector (HPGe) are often used in combination to suppress the Compton scattering background, thereby obtaining an extremely low detection limit and improving the measurement accuracy. However, the complex and expensive hardware system required does not facilitate application and promotion of this method. Thus, a method is proposed to discriminate the digital waveform of pulse signals output by a HPGe detector, whereby the Compton scattering background is suppressed and a low minimum detectable activity (MDA) is obtained without using an expensive and complex anti-coincidence detector and device. The electric field strength distribution and the energy deposition distribution in the detector are simulated to determine the relationship between the pulse shape and location of energy deposition, as well as the characteristics of the energy deposition distribution for full- and partial-energy deposition events. This relationship is used to develop a pulse shape discrimination (PSD) algorithm based on employing an artificial neural network (ANN) for pulse feature identification. To accurately determine the relationship between the deposited energy of gamma ( $\gamma$ )-rays in the detector and deposition location, we extract four shape parameters from the pulse signals output by the detector. Machine learning is used to input the four shape parameters to the detector. Then, the pulse signals are identified and classified to discriminate between partial- and full-energy deposition events, and some partial-energy deposition events are removed to suppress Compton scattering. The proposed method effectively lowers the MDA of a HPGe  $\gamma$ -energy dispersive spectrometer. Test results show that the Compton suppression factors for energy spectra obtained from measurements on  $^{152}\text{Eu}$ ,  $^{137}\text{Cs}$  and  $^{60}\text{Co}$  radioactive sources are 1.13 (344 keV), 1.11 (662 keV) and 1.08 (1332 keV), respectively, and the corresponding MDAs are lowered by 1.4%, 5.3% and 21.6%.

**Keywords:** High-purity germanium  $\gamma$ -ray spectrometer; Pulse shape discrimination; Compton scattering; Artificial

neural network; Minimum detectable activity

---

## 1. Introduction

Incomplete deposition of the energy of gamma ( $\gamma$ ) rays in a detector increases the Compton background count in  $\gamma$ -ray spectra [1] and reduces the peak-to-Compton ratio, which adversely impacts qualitative and quantitative spectral analyses. The anti-coincidence technique is often used for Compton suppression [2-10]. However, one or more anti-coincidence detectors with electronic circuits are required, which increases the system volume, equipment complexity and maintenance costs. Pulse shape discrimination (PSD) is also used for Compton suppression [11-15] and can lower Compton scattering background without the use of an anti-coincidence detector and anti-coincidence electronic circuits. The instrument used for PSD can be designed and manufactured by a simple process, is easy to maintain and has a low failure rate and cost. PSD is widely applicable to portable and laboratory radiation detection instruments. Therefore, an increasing number of researchers have been using PSD to suppress the Compton scattering background.

Classical PSD methods, such as the PSD method based on A/E features, the PSD method based on the trailing edge of the current waveform, and the PSD method based on the rising time ratio of the charge waveform, can achieve background suppression by screening single- and multi- point events to enhance the peak-to-Compton ratio of the energy spectrum [14-20]. However, the suppression of background is often accompanied by the loss of full-energy peak counts. In the application of minimum detectable activity (MDA) reduction, the difficulty lies in deducting the background without or with less loss of full-energy peak counts, which requires accurate screening of event types. The results of some simulations and experimental studies show that the pulse shape output by a preamplifier is not only affected by single- and multi-point events, but also depends strongly on the location of energy deposition in the detector [21-29]. Thus, the difference in the location of energy deposition has an impact on the accuracy of event type identification. In the low-energy zone of a detector, there is a high probability that the photoelectric effect will occur, such that removal of single-point events increases the likelihood of removing full-energy deposition events using traditional PSD [30]. Therefore, there is no literature indicating that the PSD method applied to the high-purity germanium (HPGe) detection system has achieved good results in background suppression in the low-energy region. In addition, the pulse waveform reflects a variety of physical factors such as interaction type, energy deposition location, etc., and has a certain degree of complexity [31-34]. Multiple physical features of the waveform can describe the waveform shape more finely and provide more effective information for event type identification, thus improving the accuracy of event type identification.

In this study, the relationship between the pulse shape and location of energy deposition is determined and the

energy deposition location is used to discriminate the event type. The multi-parameter concept is introduced to provide more effective information for event type identification, and the artificial neural network technique is combined to screen the event types, which effectively improves the accuracy of event type identification, enhances the peak-to-Compton ratio of the energy spectrum, and reduces the MDA by deducting a large amount of background while losing very few full-energy peak counts.

## 2. Method and Simulation

### 2.1 Modeling the detector

To investigate the relationship between the energy deposition location and the pulse shape, SolidStateDetectors.jl [35] is used to model and simulate the HPGe detector. The coaxial type HPGe detector has a diameter of 63.6 mm, a height of 59.8 mm, an electrode diameter of 7.5 mm, and an electrode height of 43.5 mm. The three-dimensional structure is shown in Figure 1. The anode potential is 0 V, the cathode potential is -2200 V, and the bias voltage is 2200 V. The operating environment temperature is 78K. A cylindrical impurity concentration distribution model that varies radially and vertically, with a central impurity concentration of  $5.8 \times 10^9 \text{ atoms} \cdot \text{cm}^{-3}$  and an impurity concentration near the cylindrical edge of  $\sim 6.2 \times 10^9 \text{ atoms} \cdot \text{cm}^{-3}$  is configured as a parameter in the simulation environment.

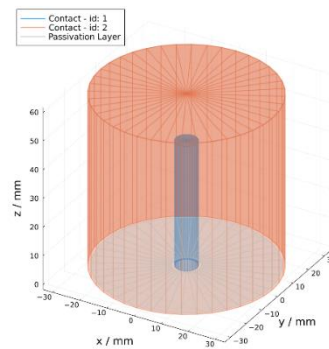


Fig. 1 The three-dimensional structure of high-purity germanium detector.

### 2.1 Field Strength Simulation

The electric field  $\vec{E}$  is one of the two components required to calculate the drift trajectory of charge carriers. To calculate the electric field, it is necessary to solve the Poisson equation for the electric potential  $\phi(\vec{r})$ :

$$\nabla^2 \phi(\vec{r}) = \frac{-\rho(\vec{r})}{\epsilon_0 \epsilon_r} \quad (1)$$

where  $\rho(\vec{r})$  represents the spatial charge density,  $\varepsilon_0$  denotes the dielectric constant, and  $\varepsilon_r$  represents the dielectric distribution.

The calculation formula for the electric field  $\vec{E}$  is given by

$$\nabla \vec{E} = \frac{\rho(\vec{r})}{\varepsilon_0 \varepsilon_r} \quad (2)$$

The open-source software package SolidStateDetectors.jl solves for the electric potential and electric field strength in each grid within the detector using the above equation through the successive over-relaxation (SOR) algorithm. It obtains the values of electric potential and electric field strength and visualizes their distributions, generating contour plots for equipotential lines and electric field lines. The results are shown in Figure 2.

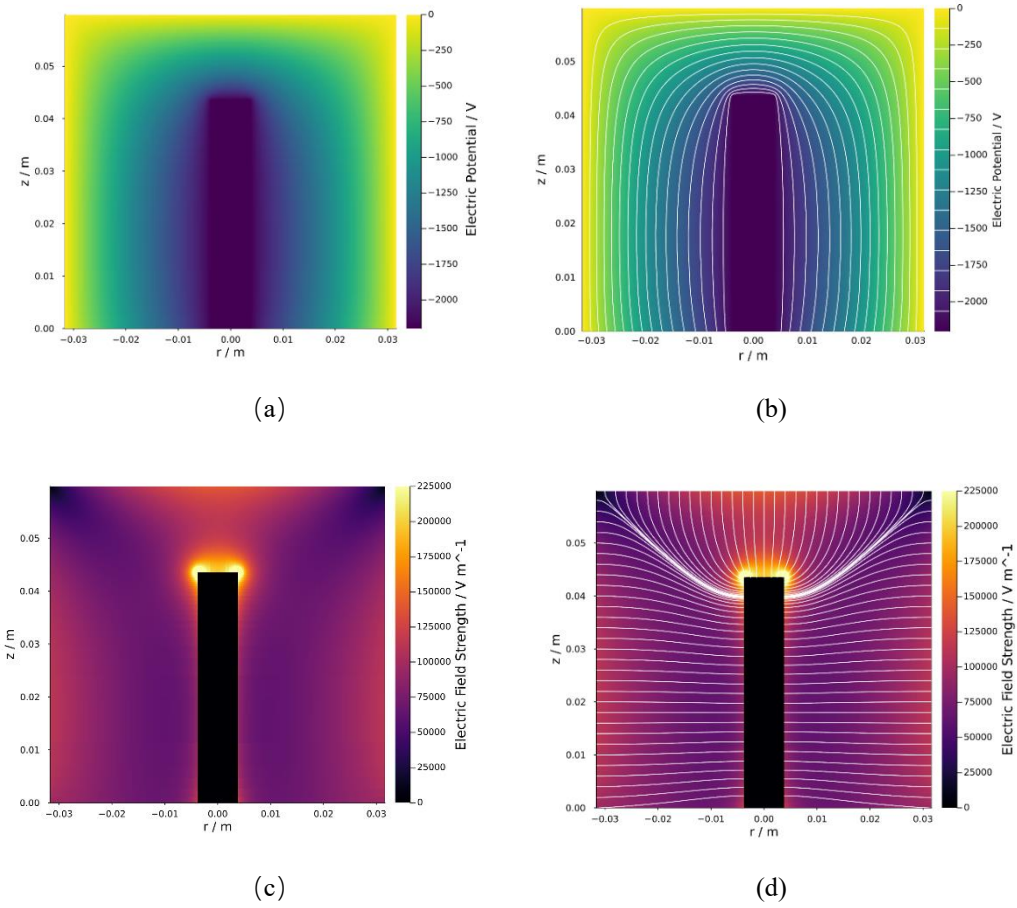


Fig. 2 The distribution of (a) potential, (b) potential with equipotential lines, (c) electric field strength, and (d) electric field strength with electric field lines of high-purity germanium detector.

To calculate the weighting potential distribution of the germanium crystal and determine the induced signals on the electrodes during the charge carrier drift process, we can solve the weighted potential  $\phi(\vec{r})$  using the Poisson equation with boundary conditions. Assuming that the anode has a weighting potential of 1 V, and the cathode has a weighting potential of 0 V.

$$\phi(\vec{r}) = \begin{cases} 1 \text{ V} & \forall \vec{r} \in C_{col} \\ 0 \text{ V} & \forall \vec{r} \in C_{uncol} \end{cases} \quad (3)$$

$C_{col}$  represents the charge collection electrode, while  $C_{uncol}$  represents the non-charge collection electrode. Setting the space charge to zero, the weighting potential distribution inside the detector is obtained through multiple iterations of SOR solving calculations, as shown in Figure 3.

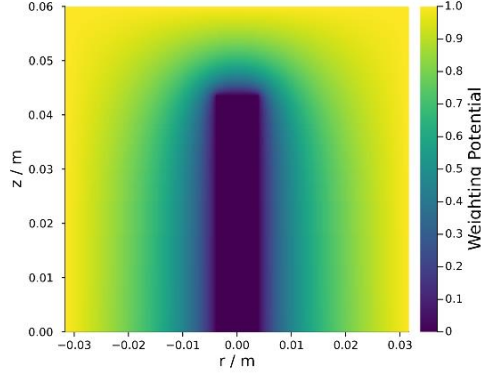


Fig. 3 The distribution of weighting potential of high-purity germanium detector.

### 2.3 Drift velocity model

The relationship between the drift velocity vector  $\vec{v}$  and the electric field vector  $\vec{E}$  is given by the following equation:

$$\vec{v}_{e/h} = u_{e/h}(\vec{E})\vec{E}(\vec{r}) \quad (4)$$

Where  $\vec{v}_{e/h}$  represents the drift velocity of charge carriers, with  $e$  representing electrons and  $h$  representing holes, and  $u_{e/h}$  represents the mobility of charge carriers.

Due to the band structure of germanium crystals, the conductivity is anisotropic at high electric fields and low temperatures. This anisotropy leads to different values of the drift velocity of charge carriers in different directions relative to the crystal axes. Moreover, if the electric field direction does not align with the crystal's rotational symmetry axis, the drift velocity will have a non-zero angle relative to the applied electric field. The drift velocities  $\vec{v}_{e/h}$  along the crystal axes  $\langle 100 \rangle$ ,  $\langle 110 \rangle$ , and  $\langle 111 \rangle$  can be described using empirical formulas [36-38].

$$\vec{v}_{e/h} = \frac{u_0 \vec{E}}{(1 + (\vec{E}/E_0)^\beta)^{1/\beta}} - u_n \vec{E} \quad (5)$$

Where the scalar  $u_0$  represents the mobility at low electric fields.  $\vec{E}$  represents the electric field strength.  $E_0$ ,  $\beta$  and  $u_n$  are used to correct the drift velocity.

Under low electric field strength ( $0.1 \text{ kV/cm} \leq E \leq 3 \text{ kV/cm}$ ), the Gunn effect is negligible, and the mobility becomes isotropic. The fitting parameter  $u_0$  for the mobility is independent of the crystal's orientation, and the velocity formula can be simplified to equation (4). However, when  $E \geq 3 \text{ kV/cm}$ , the Gunn effect becomes significant,

and it is necessary to add the term  $u_n E$  to the formula for correction. The AGATA collaboration has determined the values of the parameters in the empirical formula for drift velocity under experimental conditions, as shown in Table 1 [37][38]. These parameters can be configured in the configuration file of the ADLChargeDriftModel, and SolidStateDetectors.jl will utilize these parameters to accurately simulate the migration velocity of charge carriers, facilitating precise simulations.

Table 1 Drift velocity model parameters developed by AGATA collaboration

Type	Direction	$\mu_0(cm^2 / Vs)$	$\beta$	$E_0(V / cm)$	$\mu_n(cm^2 / Vs)$
Electron drift	<100>	38609	0.805	511	-171
	<111>	38536	0.641	538	510
Hole drift	<100>	61824	0.942	185	-
	<111>	61215	0.662	182	-

## 2.4 Waveform simulations

In waveform simulation, the drift velocity of charge carriers at various positions within the detector is calculated based on the distribution of electric field strength and drift velocity models. The initial positions and time steps of the charge carriers are set, and the drift trajectories of the charge carriers are computed. Finally, by combining the drift trajectories with the weighting potential according to the Shockley-Ramo theorem, induced charges on the electrode are calculated, which are then converted into voltage pulse waveforms. During the waveform simulation process, charge carriers are treated as ideal point charges.

Based on the weighting potential distribution and the drift velocities of charge carriers at various positions within the germanium crystal, the Shockley-Ramo theorem can be used to calculate the signal waveform induced on the readout electrode within the detector due to the drift of charge carriers along their trajectories [39]. For an electron-hole pair created by energy deposition at a point  $r$ , with an equal and opposite static charge  $q$ , the electron drift trajectory is denoted as  $r_e$  and the hole drift trajectory as  $r_h$ . The formula for calculating the induced charge  $Q(t)$  at the electrode at time  $t$  is as follows:

$$Q(t) = -q\{\phi[r_h(t)] - \phi[r_e(t)]\} \quad (6)$$

Where  $\phi$  represents the weighting potential at the positions of  $r_e$  and  $r_h$  on the electrode at time  $t$ .

The simulated waveform amplitudes are given in units of charge  $e_0$ . For a charge-sensitive preamplifier, the induced charges on the detector electrode are integrated on the feedback capacitor and converted into a voltage signal. Meanwhile, the continuous discharge occurs on the feedback resistor. The output voltage of the preamplifier

$U_{out}(t)$  can be represented by formula (7).

$$U_{out}(t) \approx \frac{Q(t) \cdot e_0}{C_f} e^{-\frac{t}{\tau}} \quad (7)$$

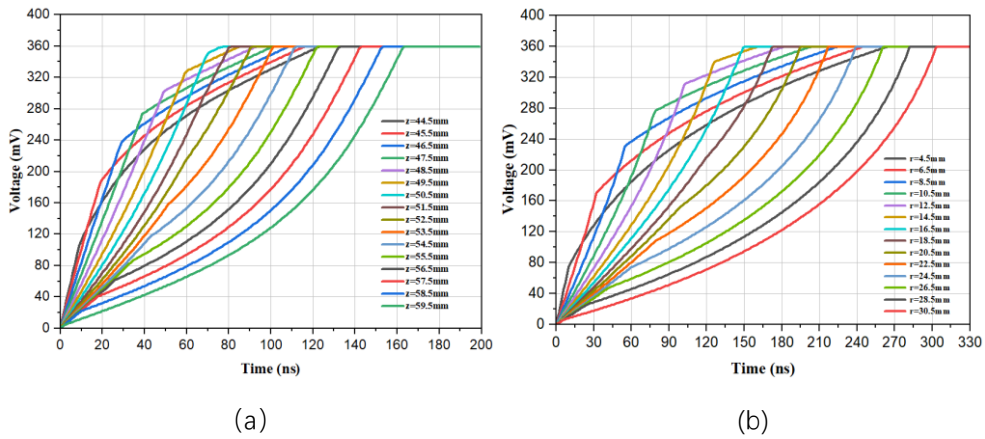
Where  $e_0$  represents the elementary charge, with a value of  $1.6 \times 10^{-19}$  C.  $C_f$  denotes the feedback capacitor, and  $\tau$  represents the time constant. In the laboratory detection system, the value of  $C_f$  is approximately 0.1 pF, and the value of  $\tau$  is 85  $\mu$ s. The rise time of pulse signal is mostly less than 400 ns. Computing  $e^{-\frac{t}{\tau}}$  to be  $0.995 \approx 1$ , we can neglect the amplitude loss of the pulse front edge voltage caused by discharge on the feedback resistor of the preamplifier. The voltage signal output by the preamplifier can be expressed by the following equation.

$$U_{out}(t) = \frac{Q(t) \cdot e_0}{C_f} \quad (8)$$

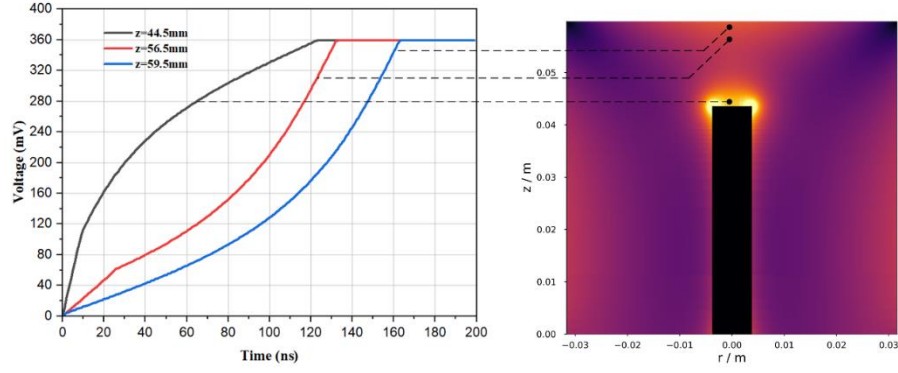
The waveforms along multiple positions along the axial and radial directions of the detector are simulated and analyzed. Along the positive direction of the cylindrical axis, the initial height of the charge carriers is set from 44.5 mm to 59.5 mm, with a step size of 1 mm for each waveform simulation. This resulted in waveforms at 16 positions, as shown in Figure 4(a). At a height of 25 mm along the cylindrical axis, along the radial direction of the cylinder, the initial position of the charge carriers is set from 4.5 mm to 30.5 mm, with a step size of 2 mm for each waveform simulation. This resulted in waveforms at 14 positions, as shown in Figure 4(b).

Three representative waveforms are selected from both the axial and radial directions to compare their shape differences, as shown in Figure 4

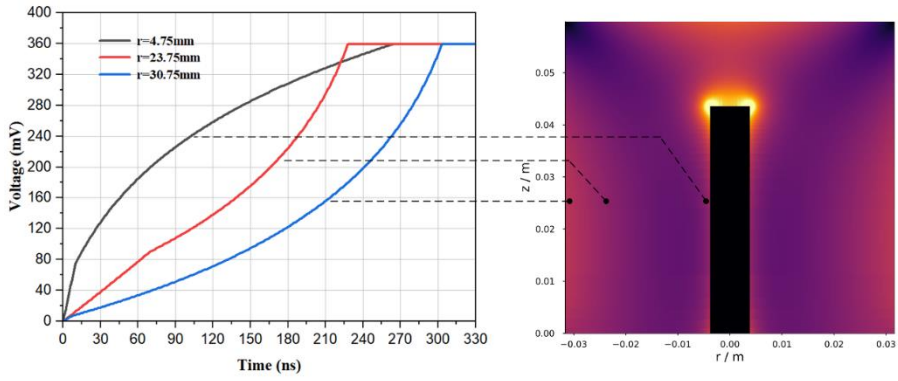
(c) and (d). In both directions, the energy deposition locations have a significant impact on the pulse waveform shape. The pulse waveform generated near the cathode exhibits a fast-to-slow rise time. On the other hand, the pulse waveform generated near the anode exhibits a slow-to-fast rise time. The pulse waveform generated at an intermediate depth position exhibits a fast-to-slow-to-fast rise time, presenting a reverse-S shape.







(c)



(d)

Fig. 4 Simulated pulse waveforms corresponding to multiple energy deposition locations in the (a) axial and (b) radial directions, and three typical pulse waveforms generated at different positions in the (c) axial and (d) radial directions.

## 2.5 Analysis of impact of the charge cloud effect

The motion of electrons and holes is not solely determined by external electric field forces. In the process of carrier drift, the diffusion and self-repulsion of charge carriers also play an important role. To simulate this, electrons and holes are no longer described as single point charges but as charge clouds composed of multiple point charges. The model incorporates diffusion and self-repulsion. Diffusion is used to model the random thermal motion of charge carriers, while self-repulsion describes the repulsive interaction between charge carriers of the same type. The model does not consider the attraction between electrons and holes.

In SolidStateDetectors.jl, there are two options for charge distribution. For a charge cloud composed of a small number of charges (less than around 50), the shell consists of a polyhedron of Plato, and the point charges are distributed on the vertices of the polyhedron. For a charge cloud with a larger number of charges (more than 50), the

point charges are evenly distributed on a regular spherical surface.

The formula for calculating the number of charge carriers generated by energy deposition in a high-purity germanium detector is as follows:

$$n = \frac{E}{\omega} \quad (9)$$

Where  $n$  is the number of charge carriers generated by energy deposition,  $E$  is the deposited energy, and  $\omega$  is the ionization energy.

At a liquid nitrogen temperature (77K), the average ionization energy of high-purity germanium is approximately 3eV. In the simulation, the deposited energy in the detector is set to 344keV, 662keV, and 1332keV, respectively. According to the formula (9), the calculated numbers of generated charge carriers are approximately 114667, 220667, and 444000, respectively. Therefore, in the simulation, the charge distribution model is set as point charges uniformly distributed on a regular spherical surface. Simultaneously, the parameter used to pass the total charge quantity in the NBodyChargeCloud function is set to the respective values mentioned above, achieving the transmission of the total charge quantity parameter.

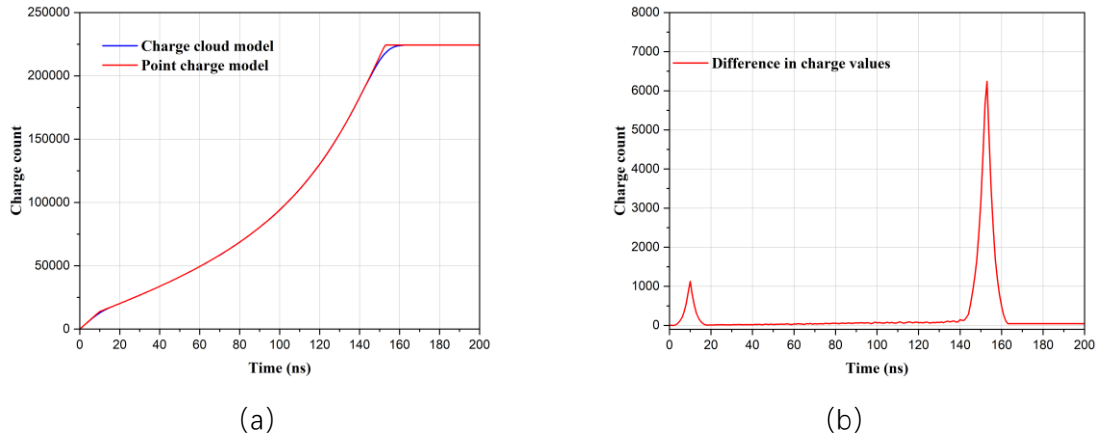


Fig. 5 (a) Charge pulse waveforms output from the electrode under the cloud charge model and point charge model when the energy deposition is 662 keV. (b): The new waveform obtained by subtracting the two pulse waveforms.

At the position  $Z=58.5\text{mm}$  on the axis (approximately 1.3mm from the top anode of the detector), the differences in the induced charge waveforms on the electrode are shown in the Figure 5 (a) for the cases with and without the charge cloud model. When electrons drift towards the anode under the influence of the electric field, the electrons that are initially close to the anode reach it first. On the other hand, holes drift towards the cathode under the electric field, and since they are initially farther away from the cathode, they arrive later.

For the point charge model, the large number of electrons produced is considered as a point arriving at the electrode at the same moment, resulting in a rapid rise in the signal at the anode. In contrast, for the charge cloud model, the large number of electrons are distributed in a spherical shape. The electrons near the boundary of the spherical cloud on the side closer to the anode reach the electrode first, followed by the electrons near the center of the sphere, and finally the electrons near the boundary on the side farther from the anode. As a result, the number of electrons reaching the electrode gradually increases, leading to a relatively slow change in the amplitude of the induced charge on the anode compared to the point charge model. The subtraction of the charge waveforms between the two models produces the first pulse shown in the Figure 5 (b). The process is similar for the drift of holes towards the cathode, resulting in the second pulse shown in the Figure 5 (b). Due to the slower drift velocity of holes, the rate of change in the amplitude of the induced charge during the collection process by the electrode is smaller for the charge cloud model compared to when electrons are collected. Therefore, the pulse amplitude after subtracting the charge waveforms between the two models is larger for holes being collected.

In summary, different models result in certain differences in the spatial distribution of charge carriers, thereby causing slight differences in the induced charge waveforms during the drifting process of charge carriers towards the electrode.

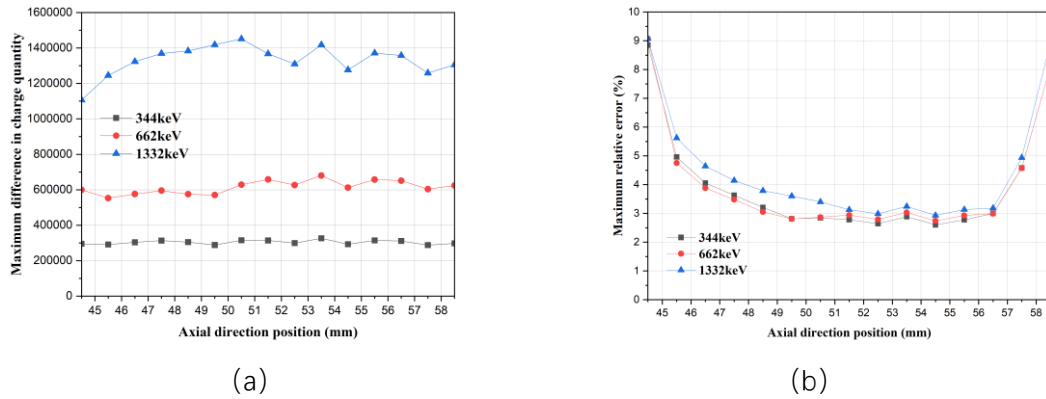


Fig. 6 (a) The trend of the maximum charge difference in the pulse waveforms generated by two models with energy depositions at different positions, for energy depositions of 344 keV, 662 keV, and 1332 keV. (b)

The trend of the maximum relative error with respect to the energy deposition position.

In the simulation, when the charge distribution model is set as the charge cloud model, there are certain changes in the waveform of the induced charge compared to the point charge model. We calculate the charge waveforms generated on the electrodes under both models, subtract them to extract the maximum difference in charge quantity,

---

and analyze the results. Simulations are conducted for energy depositions of 344 keV, 662 keV, and 1332 keV at points along the axis from a coordinate of  $z = 44.5$  mm to  $z = 58.5$  mm with a 1 mm interval. The charge waveforms under both models are calculated, and the maximum difference in charge quantity is plotted in a scatter plot as shown in Figure 6 (a).

It can be observed that the change in position does not affect the maximum difference in charge quantity under both models. However, as the energy deposition increases, the maximum difference in charge quantity increases under both models. This is because, in the charge cloud model, as the number of carriers increases, the radius and distribution density of the charge cloud also increase. With the increase in radius, it takes longer for the charge cloud to be completely collected by the electrode. With the increase in distribution density, the cardinality of the charge cloud increases, resulting in a larger difference in charge quantity under both models during the same collection process.

The Figure 6 (b) shows the maximum relative error as a measure of the influence of the charge cloud model on the pulse waveform. It can be seen that the maximum relative error is less than 5% in the range of  $z = 45.5$  mm to  $z = 57.5$  mm. In the region near the electrodes where the energy deposition position approaches, the relative error increases. This is because when the energy deposition position is close to the electrode, the electron cloud or hole cloud is rapidly collected by the electrode. The waveform data is smaller when the charge quantity reaches its maximum difference. As this smaller waveform data is used as the denominator for calculating the maximum relative error, it leads to a relatively larger calculated value. However, the values of these relative errors are still less than 10%. Based on the above analysis, the influence of the charge cloud model on the waveform shape can be considered negligible.

## 2.6 Energy deposition location simulation

We consider two types of events, i.e., full- and partial-energy deposition. In this section, we determine the relationship between the energy deposition location and event type. This relationship is used to discriminate between the two event types based on the difference in the distribution of the energy deposition location. We use the GEANT4 simulation software package [40-42] developed by the European Organization for Nuclear Research (CERN) to simulate the interaction process of 344-, 662- and 1332-keV rays from  $^{152}\text{Eu}$ ,  $^{137}\text{Cs}$  and  $^{60}\text{Co}$  radioactive sources entering a coaxial HPGe detector [43]. In the GEANT4 environment, QBBC is registered as a physics list, including

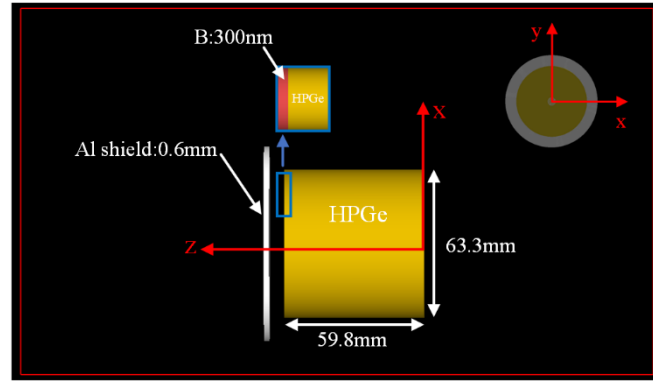
---

the G4EM standard physics package and G4DecayPhysics physics package. A detector model is established using the N-type coaxial HPGe detector used in the laboratory as a prototype. The diameter and height of the Ge crystal are 63.3 and 59.8 mm, respectively. A 0.6-mm-thick piece of aluminum placed at 6.3 mm from the top of the Ge crystal is used to simulate the aluminum shell of the detector. A 300-nm-thick borided layer is used as a thin window on top of the Ge crystal. The dimensions and positions of the HPGe crystal and aluminum shell are shown in Figure 7 (a). The radiation source is a planar source with a circular shape, centered on the detector axis, and a diameter of 63.3 mm. It is located 40 mm above the surface of the detector. During the simulation, 200,000 gamma rays with energies of 344 keV, 662 keV, and 1332 keV are respectively emitted along the negative z-axis as incident rays. The initial position and direction of the gamma rays are shown in Figure 7 (b). In the Geant4 simulation, the gamma rays first pass through the aluminum casing and thin window, and then interact with the germanium crystal. The transport processes, reaction types, and interaction points at the step level inside the germanium crystal are statistically analyzed in the simulation. For each event, conditional statements are used to select events with partial-energy deposition and events with full-energy deposition, and to extract the coordinates of the last energy deposition. The event type selection and coordinate extraction are performed in the Geant4 program file SteppingAction.cc. The selection criteria for event types are as follows:

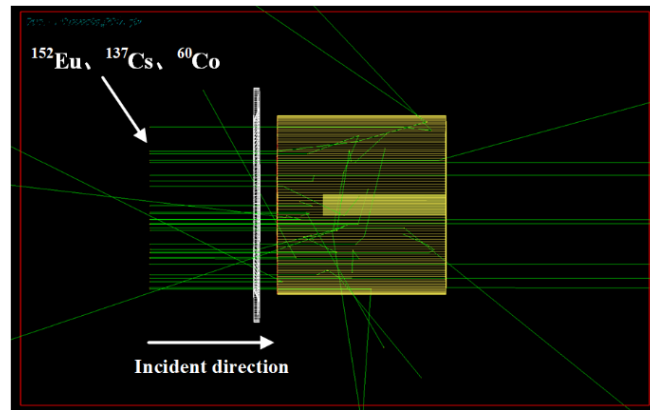
Partial-energy deposition event criteria: The previous energy deposition position is within the germanium crystal material, the subsequent ray passes through the boundary between the germanium crystal and the medium material, and the kinetic energy of the ray when passing through is greater than 0.

Full-energy deposition event criteria: The previous energy deposition position is within the germanium crystal material, and the kinetic energy of the ray afterwards is 0.

After the simulation, the number of incident rays, the total number of energy deposition events, the number of full-energy deposition events, and the number of partial-energy deposition events are recorded. The results are shown in Table 2. The coordinate values of the two types of events are processed into radius and height, resulting in the position distribution of the interactions in the HPGe detector for both types of events, as shown in Figure 8.



(a)

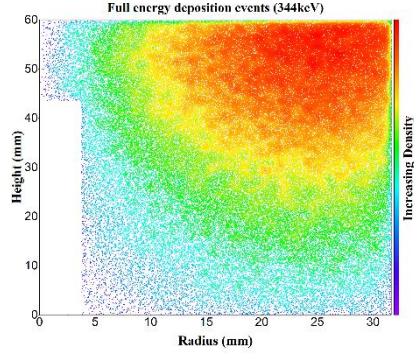


(b)

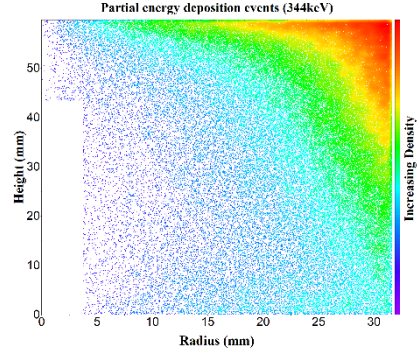
Fig. 7 (a) Model of the coaxial HPGe detector simulated using Geant4. (b) Process of energy deposition of gamma rays in the HPGe detector.

Table 2 Data statistics obtained from the Geant4 simulation

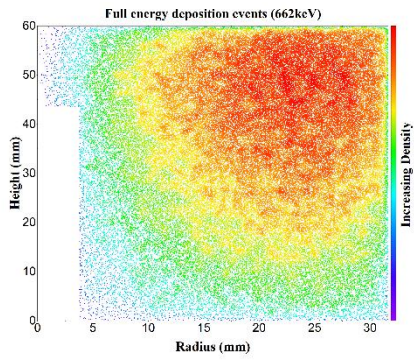
Nuclide	Energy (keV)	Number of incident rays	Total number of energy deposition events	Number of full-energy deposition events	Number of partial- energy deposition events
$^{152}\text{Eu}$	344	200000	140921	128755	12166
$^{137}\text{Cs}$	662	200000	103279	82306	20973
$^{60}\text{Co}$	1332	200000	67889	51871	16018



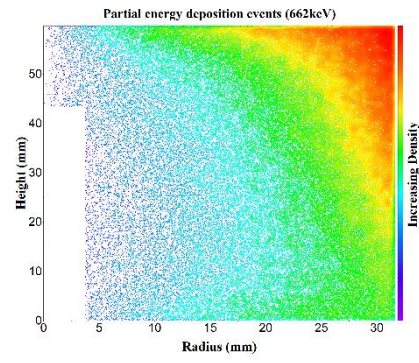
(a)



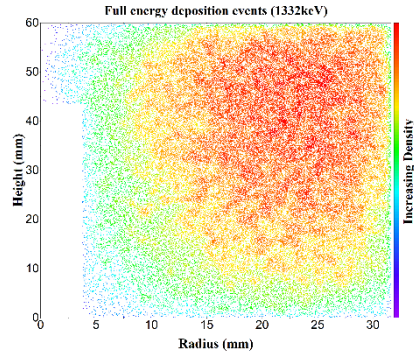
(b)



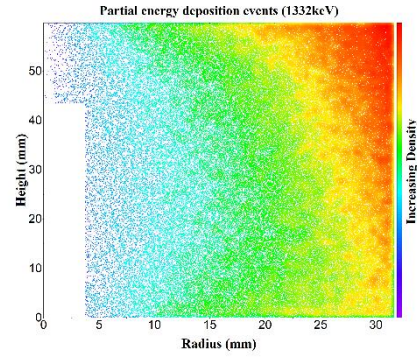
(c)



(d)



(e)



(f)

Fig. 8 Distribution of locations of full-energy deposition events ((a), (c) and (e)) and partial-energy deposition events ((b), (d) and (f)) corresponding to the interaction of 344-, 662- and 1332-keV  $\gamma$ -rays with the detector.

The simulation results show that the full-energy deposition events are concentrated deep in the detector, whereas the partial-energy deposition events mostly occur at the detector surface. Thus, we can identify the event type by the deposition location of  $\gamma$ -ray energy in the detector.

In this section, we have analyzed the relationship among the pulse shape, energy deposition location and event

---

type, as well as the mechanism that causes interconnection of these three factors.

### 3. Data processing algorithm

By combining the PSD method with machine learning, a more accurate event identification can be achieved. A PSD algorithm based on artificial neural network (ANN) pulse feature recognition has been proposed. This algorithm utilizes four features of the leading-edge waveform of the pulse signal as decision parameters. The four features of the pulse waveform provide more useful information for event type identification, thus improving the accuracy of event type identification. The four features make different contributions to the identification of event type, i.e., the features have different weights. It is difficult to reasonably allocate weights for the decision parameters manually. Thus, machine learning is employed to train the ANN. Training algorithm enables continual improvement of the weights in the network. The model with the optimal weights has the highest accuracy for discriminating the event type and thus, the highest performance for discriminating Compton scattering events. The model training process consists of three stages. In the first stage, the effective range of the leading edge is determined from the pulse signals. In the second stage, the PSD algorithm is used to extract the four decision parameters from the effective range of the leading edge. In the third stage, an ANN model is built and a dataset is constructed.

#### 3.1 Data stripping

Gamma rays deposit energy in the detector, generating electron-hole pairs that undergo drift under the influence of an electric field, which is manifested in the rising phase of the charge-sensitive preamplifier output. Therefore, we extract the leading-edge waveform from the original waveform for analysis. The total number of sampling points for each leading-edge waveform is  $N_{\text{Total}}$ . Before applying the PSD algorithm, we preprocess the leading-edge waveform.

The amplitude of the leading edge of the pulse signal  $P_{\text{AMP}}$  is calculated as the peak amplitude  $P_{\text{PEAK}}$  minus the baseline amplitude  $P_{\text{BASE}}$ .

$$P_{\text{AMP}} = P_{\text{PEAK}} - P_{\text{BASE}} \quad (10)$$

A prescribed percentage of the leading-edge amplitude is extracted to obtain an effective signal range to reduce noise interference and prevent time walking of the amplitude [44]. The dynamic upper limit  $TH_{\text{UP}}$  and dynamic lower limit  $TH_{\text{LW}}$  are used to obtain the effective signal range:

$$TH_{\text{UP}} = r_{\text{UP}} \cdot P_{\text{AMP}} + P_{\text{BASE}} \quad (11)$$

$$TH_{\text{LW}} = r_{\text{LW}} \cdot P_{\text{AMP}} + P_{\text{BASE}} \quad (12)$$

where  $r_{\text{UP}}$  and  $r_{\text{LW}}$  are the upper and lower percentages of the leading-edge amplitude, respectively. In this study,



$r_{UP}$  and  $r_{LW}$  are set to 90% and 10% to calculate the dynamic threshold, and the resulting effective signal range is shown in Figure 9. The gain of the digital signal is approximately 12.6 LSB/keV, where LSB denotes the least significant bit of the ADC.

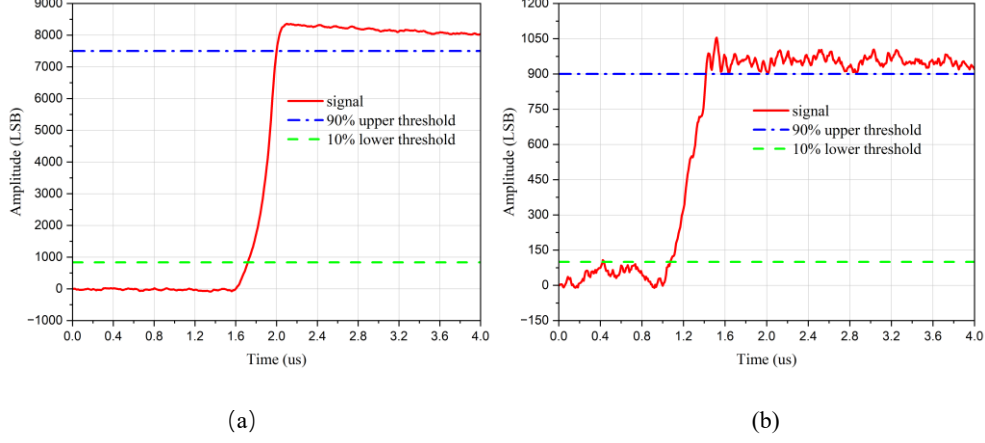


Fig. 9 (a) and (b) show the sampling waveform at the leading edge and the corresponding upper and lower thresholds. The equivalent energy of the pulse signal is (a) ~662 keV and (b) ~74 keV.

However, for small-amplitude signals, baseline noise may trigger the lower threshold before the signal leading edge, as shown in Figure 9 (b). To prevent such false triggers, we use the reverse signal sampling sequence to capture the trigger sequence number for the lower threshold and the normal pulse sampling sequence to capture the trigger sequence number of the upper threshold. The trigger sequence numbers of the upper and lower thresholds should satisfy the following inequality:

$$P[M' - 1] > TH_{LW}, \text{ and } P[M'] < TH_{LW} \quad (13)$$

$$P[N] < TH_{UP}, \text{ and } P[N + 1] > TH_{UP} \quad (14)$$

Where  $P[n]$  is the waveform of leading edge.  $M'$  is the sequence number in the reverse sampling sequence when the sampling point is just less than the lower threshold, and  $N$  is the sequence number in the forward sampling sequence when the sampling point is just less than the upper threshold.  $M'$  is converted to the corresponding sequence number  $M$  in the forward sampling sequence by Equation (15).

$$M = N_{Total} - M' \quad (15)$$

After obtaining the sequence numbers  $M$  and  $N$ , the waveform  $w[n]$  within the effective signal range of the leading edge is determined, as described below.

$$w[n] = P[M + n - 1] - P[M], \quad n = 1, 2, \dots, N - M + 1 \quad (16)$$

### 3.2 Feature extraction

Processing is carried out using the PSD algorithm as follows. First, the slope of the effective signal (which has been extracted as described in the preceding section) is calculated. Then, the corresponding slope amplitude is subtracted from each discrete signal amplitude within the effective signal interval to determine a new set of discrete signals. The decision parameters are taken to be the maximum value of the new discrete signal and the corresponding relative position on the curve, as well as the minimum value of the new discrete signal and the corresponding relative position on the curve. These four decision parameters accurately reflect the shape features of pulse signals.

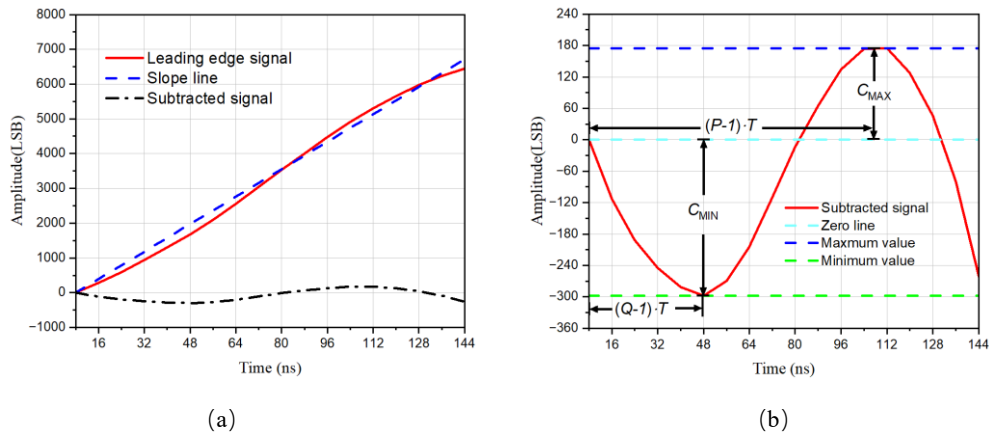


Fig. 10 (a) and (b) Processing procedure of the pulse shape discrimination algorithm.

Many methods, such as curve fitting, can be used to calculate the slope of the leading edge. To simplify the signal processing process, the slope of the leading edge is calculated using the formula given below:

$$K_{\text{SLOPE}} = \frac{w[N-M+1]}{T_{\text{TOTAL\_TIME}}} \quad (17)$$

$$T_{\text{TOTAL\_TIME}} = (N - M) \cdot T \quad (18)$$

where  $T_{\text{TOTAL\_TIME}}$  is the total time of the effective signal range and  $T$  denotes the sampling period, i.e., 8 ns.

The discrete signal of the new curve  $f[n]$  is obtained by subtracting the discrete value of the slope from the discrete value of the effective range of the leading edge.

$$f[n] = w[n] - (n - 1) \cdot T \cdot K_{\text{SLOPE}} \quad (19)$$

The maximum value  $C_{\text{MAX}}$  and minimum value  $C_{\text{MIN}}$  of the curve that reflects the protruding degree (upward and downward) of the effective range of the leading edge are calculated using the formula given below:

$$C_{MAX} = w[P] - (P - 1) \cdot T \cdot K_{SLOPE} \quad (20)$$

$$C_{MIN} = w[Q] - (Q - 1) \cdot T \cdot K_{SLOPE} \quad (21)$$

where P and Q are the numbers at the maximum and minimum of the curve, respectively. The relative positions of P and Q at the leading edge are

$$R_{MAX} = \frac{P-1}{N-M} \quad (22)$$

$$R_{MIN} = \frac{Q-1}{N-M} \quad (23)$$

The maximum upper and lower convex values  $C_{MAX}$  and  $C_{MIN}$  within the effective range of the leading edge and the corresponding relative positions  $R_{MAX}$  and  $R_{MIN}$  at the leading edge are used as the four decision parameters of the pulse signals.

### 3.3 Analysis of the impact of noise on decision parameters.

We have performed data analysis on simulated waveforms to assess the impact of different signal-to-noise ratio (SNR) levels, specifically 30dB, 40dB, and 50dB, on decision parameters. Waveforms are obtained at 16 positions with a 1mm interval along the axial direction from 44.5mm to 59.5mm. Different levels of noise are added to the original waveforms to achieve SNRs of 30dB, 40dB, and 50dB for each signal. The PSD algorithm is then used to extract the decision parameter values for each signal. The mean square deviation of each decision parameter for each signal group is calculated and plotted as a scatter plot, as shown in Figure 11. The decreasing trend of the mean square deviation with increasing SNR indicates that noise has a certain degree of influence on the values of the decision parameters. Therefore, in the experimental process, efforts should be made to minimize system noise.

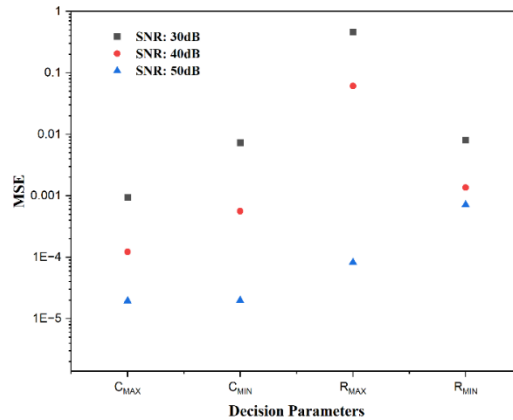


Fig. 11 Mean square error of the effect of different levels of noise on the decision parameters.

### 3.4 ANN

Artificial Neural Networks (ANNs) are modern and powerful classification tools [45] that can be used as

classifiers to distinguish pulse shapes. In the experiment, a two-layer feedforward neural network is employed as an artificial neural network model. The model consists of an input layer with 4 inputs, a hidden layer with 10 neurons, and an output layer with 2 neurons. The activation function for the hidden layer is the sigmoid function. The training algorithm used is the Levenberg-Marquardt backpropagation algorithm. The data outputted from the output layer can be interpreted as the probability that the model predicts the event type as full-energy deposition event. The structure of the artificial neural network is shown in Figure 12. Based on four decision parameters extracted from the pulse waveform, the artificial neural network computes the predicted probability of the pulse waveform belonging to a particular event type. The closer the result is to 1, the higher the probability that the event belongs to the full-energy deposition event. On the other hand, the closer the result is to 0, the higher the probability that the event belongs to the partial-energy deposition event. By setting a threshold, events with a prediction above the threshold are retained, while events with a prediction below the threshold are excluded, aiming to maximize the retention of full-energy deposition event and exclude partial-energy deposition events.

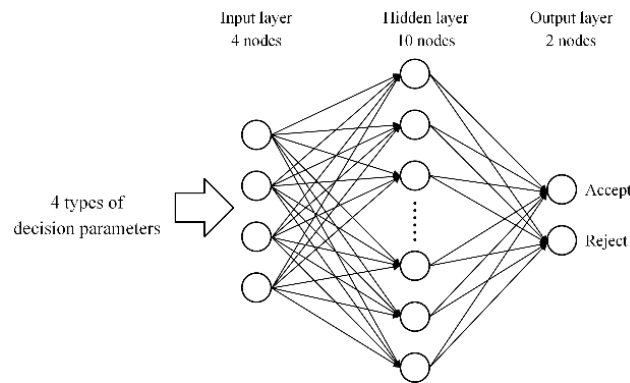


Fig. 12 Block diagram for the ANN structure.

## 4. Results and Discussion

### 4.1 Detector system

The full-waveform acquisition and analysis system for the HPGe signal used in this study is composed of a compartment with a lead shield, coaxial HPGe detector, high-voltage module, signal conditioning circuit, full-waveform digital acquisition board, computer and upper computer software. A GCDX-40190 N-type coaxial HPGe detector manufactured by BSI in Sweden is used. The detector has a relative efficiency of 40% and an energy resolution of 1.9 keV@1332 keV. The diameter and height of the HPGe crystal are 63.3 and 59.8 mm, respectively, and the diameter of cathode electrode is 7.5 mm. The detector is placed in the lead compartment, which has a thickness of 10 cm to reduce interference from the environmental background. The lead compartment contains a

copper baffle to block X-rays emitted by lead decay. The radioactive sources include  $^{152}\text{Eu}$ ,  $^{137}\text{Cs}$  and  $^{60}\text{Co}$ . The three radioactive sources are placed on the surface right above the detector for measurement. The cathode and anode biases of the HPGe detector are -2200V and 0 V, respectively. The signal conditioning circuit scales and adjusts the bias for the pulse signals output from the preamplifier. The full-waveform digital acquisition board with a 16-bit resolution and a 125-Msps sampling rate transmits the acquired waveform data to the computer through the PCIe interface and records the data on storage media. The waveform data from the leading edge of pulse signal is extracted as the original data for subsequent study. Figures and a framework diagram of the system are shown in Figure 13.

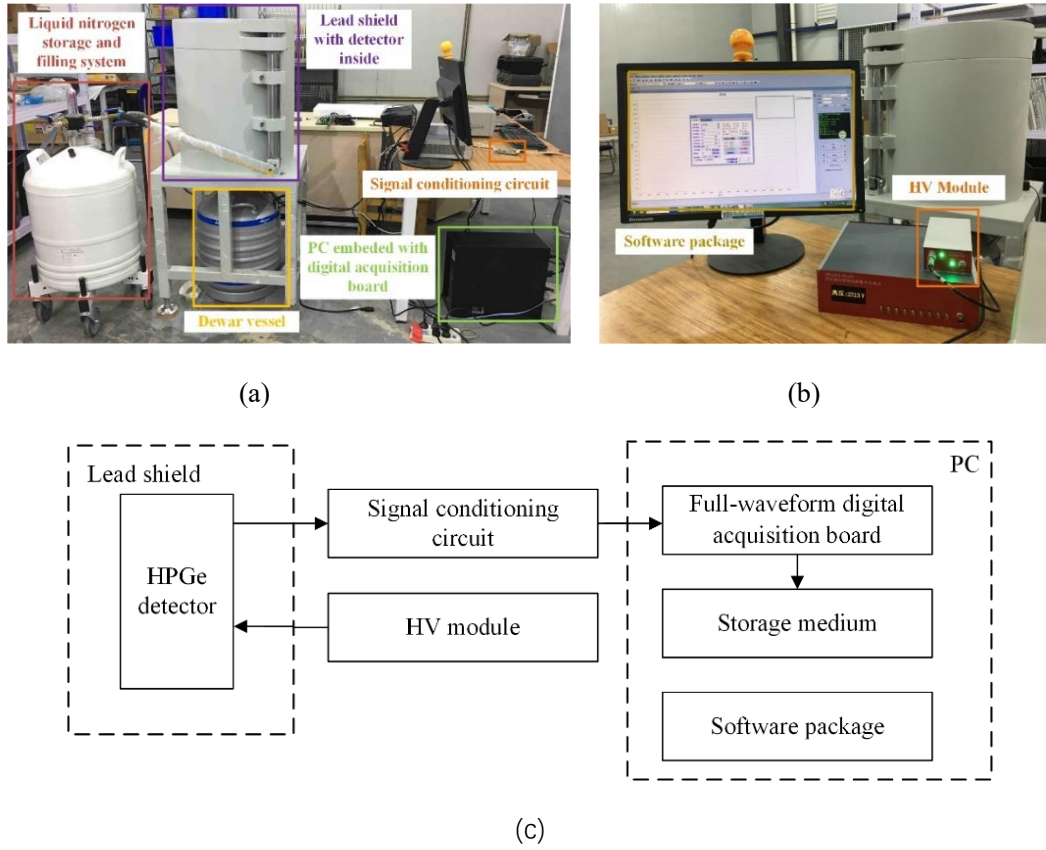
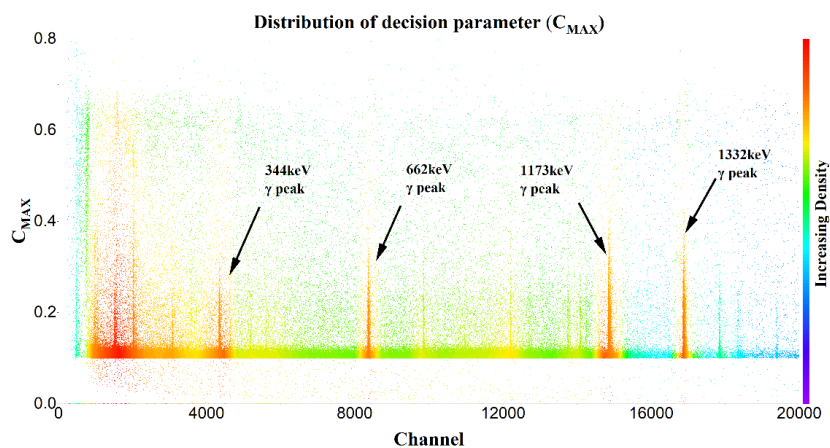


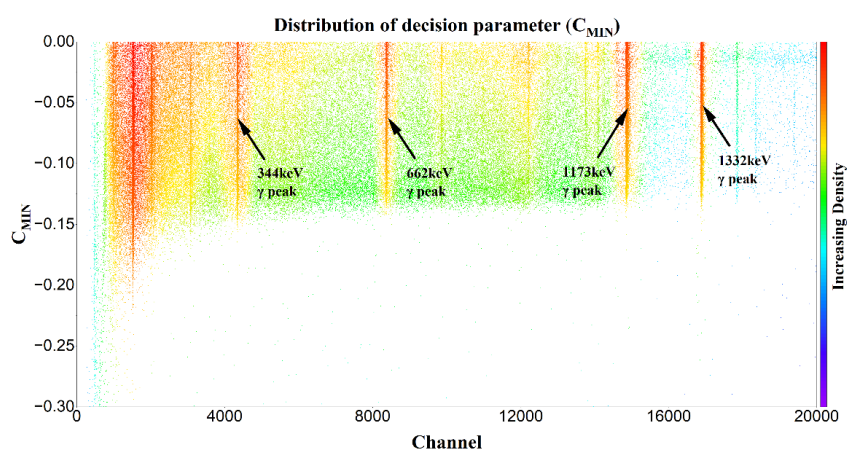
Fig. 13 Full-waveform acquisition and analysis system for the high-purity germanium signal. (a) and (b) figures and (c) framework diagram.

## 4.2 Data preprocessing

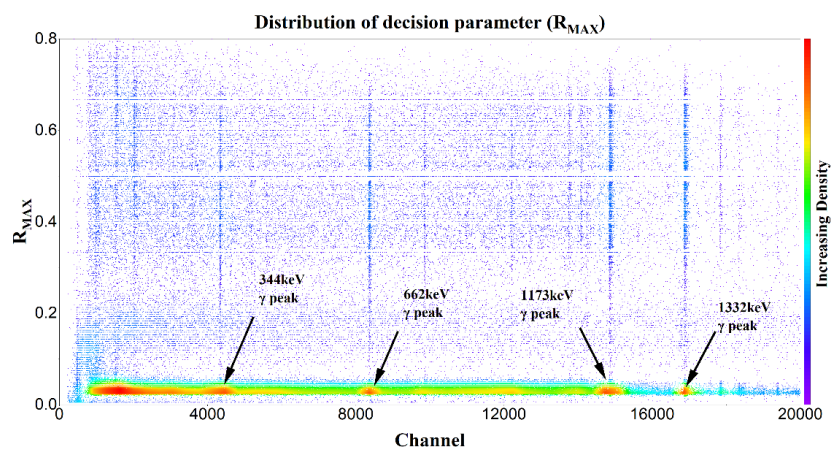
A total of 200,000 pulse signals from mixed sources of  $^{152}\text{Eu}$ ,  $^{137}\text{Cs}$  and  $^{60}\text{Co}$  are analyzed. Four eigenvalues,  $C_{\text{MAX}}$ ,  $C_{\text{MIN}}$ ,  $R_{\text{MAX}}$  and  $R_{\text{MIN}}$ , are extracted as decision parameters. Figure 14 shows a dot density map of the distribution of the decision parameters for each track address. The distributions of the decision parameters for the two event types are different and can be used to distinguish the event



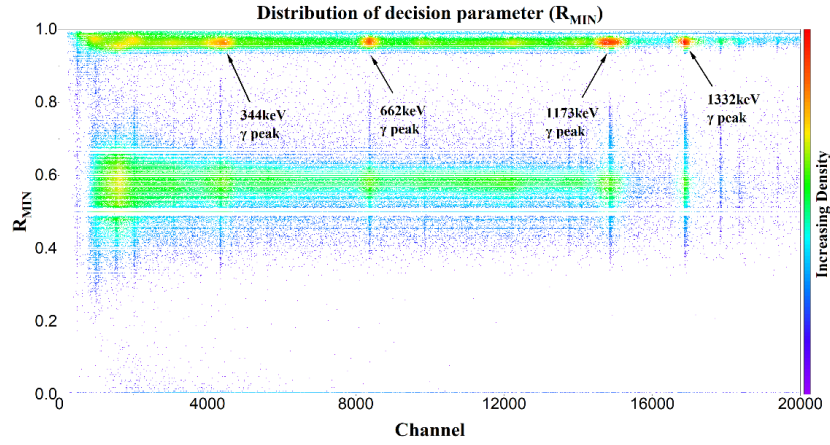
(a)



(b)



(c)



(d)

Fig. 14 Distribution of decision parameters of pulse signals from mixed radioactive sources of  $^{152}\text{Eu}$ ,  $^{137}\text{Cs}$  and  $^{60}\text{Co}$  in the corresponding track address.

#### 4.3 ANN training

Different weights are assigned to the four decision parameters to determine the event type. Extensive iterative training of the ANN on a training dataset is required to determine the optimum weight factors. A dataset containing correctly classified waveforms obtained from measurements in a laboratory environment is prepared to train the ANN using supervised learning. This dataset comprises 207724 sets of decision parameters extracted from pulse signals generated by the interaction of the detector with  $\gamma$ -rays of  $^{152}\text{Eu}$  (344 keV),  $^{137}\text{Cs}$  (662 keV) and  $^{60}\text{Co}$  (1332 keV) and the flag values. A total of 29154 sets of full-energy deposition events within the range of the full-energy peak are assigned a value of 1, and 178570 sets of partial-energy deposition events within the range of the Compton plateau are assigned a value of 0. The dataset composition is shown in Table 3. The dataset is randomly divided into three subsets containing 90%, 5% and 5% of the data for training, validation and testing, respectively. The network is constructed using the neural network toolbox in MATLAB software. The training algorithm used is the Levenberg-Marquardt backpropagation algorithm, and the initial learning rate is encapsulated in the artificial neural network toolbox. During the model training process, the learning rate is adaptively adjusted based on the training performance. The network model is trained for 126 epochs on an eight-core workstation. The trained network is employed to classify events in 89023 newly sampled and extracted datasets.

Table 3 Composition of events in the neural network model training set

Nuclide	Energy (keV)	Total number of datasets	Total number of events in a single-source dataset	Number of full- energy deposition	Number of partial- energy deposition
---------	-----------------	-----------------------------	--	--------------------------------------	---

			events	events
$^{152}\text{Eu}$	344	52941	4108	48833
$^{137}\text{Cs}$	662	207724	82134	18749
$^{60}\text{Co}$	1332	72649	6297	66352

#### 4.4 Validation of pulse shape simulation

Simulations are performed to obtain the pulse waveforms generated by the energy deposition of 662 keV gamma rays at multiple positions along the radial and axial directions within the detector. Four decision parameters are extracted from the simulated waveforms and feed into the neural network model for prediction. The depth of the energy deposition position from the detector surface and the predicted probability values of event types are plotted as a scatter plot, as shown in the Figure 15. In the figure, 'Probability' represents the probability of an event being predicted as a full-energy deposition event. A higher value indicates a higher probability of a full-energy deposition event, while a lower value suggests a higher probability of a partial-energy deposition event. It can be observed that, regardless of the radial or axial direction, when the depth is shallow, indicating a position close to the detector surface, the predicted probability of a full-energy deposition event is small. As the depth increases, the predicted probability gradually increases and reaches a maximum value at a certain depth, after which the probability value decreases.

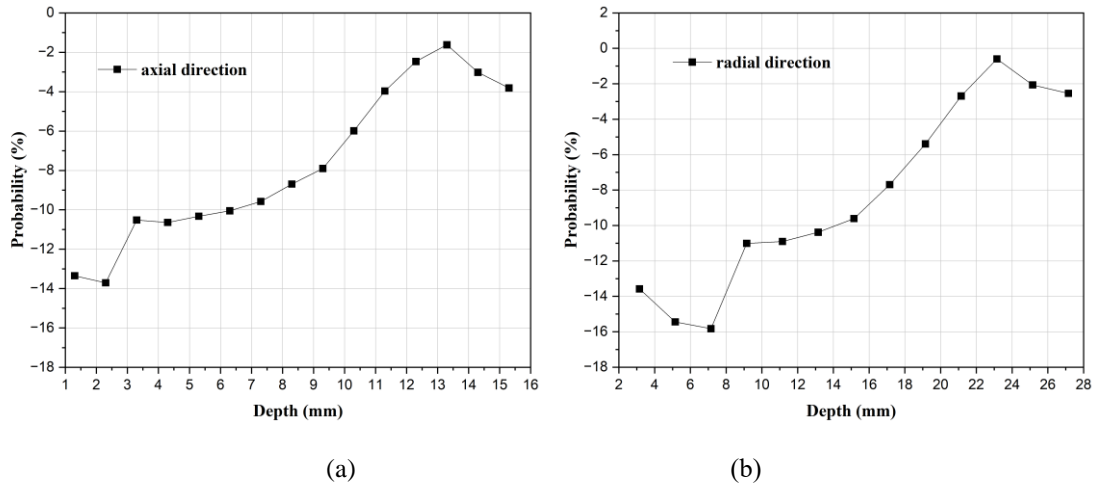


Figure 15. Scatter plots of probability values against energy deposition depth for (a) axial and (b) radial directions.

The observed trend aligns with the distribution characteristics of full/partial-energy deposition events simulated in the GEANT4 environment, as shown in the Figure 8. Partial-energy deposition events exhibit a higher probability of being distributed on the outer surface of the detector, while full-energy deposition events show a higher probability of being distributed in deeper regions of the detector. As the depth increases, the distribution probability reaches its



---

maximum value at a certain depth. As the depth approaches the cathode, the probability of gamma rays scattering and escaping the germanium crystal into the cathode increases. This leads to a decrease in the probability of full-energy deposition events. This feature aligns with the trend observed in the curves shown in the Figure 15.

The probability values on the vertical axis in the figure are generally lower than the probability values obtained through inference using measured waveform data in the experimental environment. This may be attributed to the experimental environment being more complex than the simulation environment, with more factors influencing the pulse waveform, such as the impact of the dead layer, hole trapping effects, electronic noise, etc. These factors contribute to certain differences between the waveform observed in experimental measurements and the simulated waveform. However, by training the neural network model based on the decision parameters extracted from the measured waveforms obtained in the experimental environment and redefining the thresholds, the same model can analyze and infer from the decision parameters extracted from the simulated waveforms. This indicates that the waveform shapes obtained from both simulated and experimental environments exhibit a certain degree of similarity, and the trend of changes in waveform shape characteristics remains consistent with the variation of energy deposition positions.

#### 4.5 Energy spectrum test

After the pulse-signal amplitudes of the Compton scattering events identified by the ANN are removed, the pulse-signal amplitudes of the remaining events are processed to yield an energy spectrum in which the Compton scattering background has been suppressed. The suppression effect of the Compton scattering background is quantified in terms of the Compton suppression factor ( $F_{CS}$ ) and efficiency ( $Eff$ ), which are calculated as follows:

$$F_{CS} = \frac{P/C_{CS}}{P/C_{original}} \quad (24)$$

$$Eff = F_{CS} \cdot \sqrt{R_{P-P}} \quad (25)$$

where  $P/C_{original}$  and  $P/C_{CS}$  are the peak-to-Compton ratio of the energy spectrum before and after Compton suppression using ANN, respectively, and  $R_{P-P}$  denotes the ratio of the areas of the full-energy peak in the energy spectrum before and after Compton suppression using ANN.

The following ratios are calculated: the ratio of the 344-keV full-energy peak height for signals from the  $^{152}\text{Eu}$  radioactive source to the average height of the Compton continuum at 298 keV~339 keV; the ratio of the 662-keV full-energy peak height for signals from the  $^{137}\text{Cs}$  radioactive source to the average height of the Compton continuum at 680 keV~730 keV; and the ratio of the 1332-keV full-energy peak height for signals from the  $^{60}\text{Co}$  radioactive

source to the average height of the Compton continuum at 1040 keV~1096 keV. Figure 16 presents the effect of the threshold value on the Compton suppression factor, peak area ratio and efficiency.

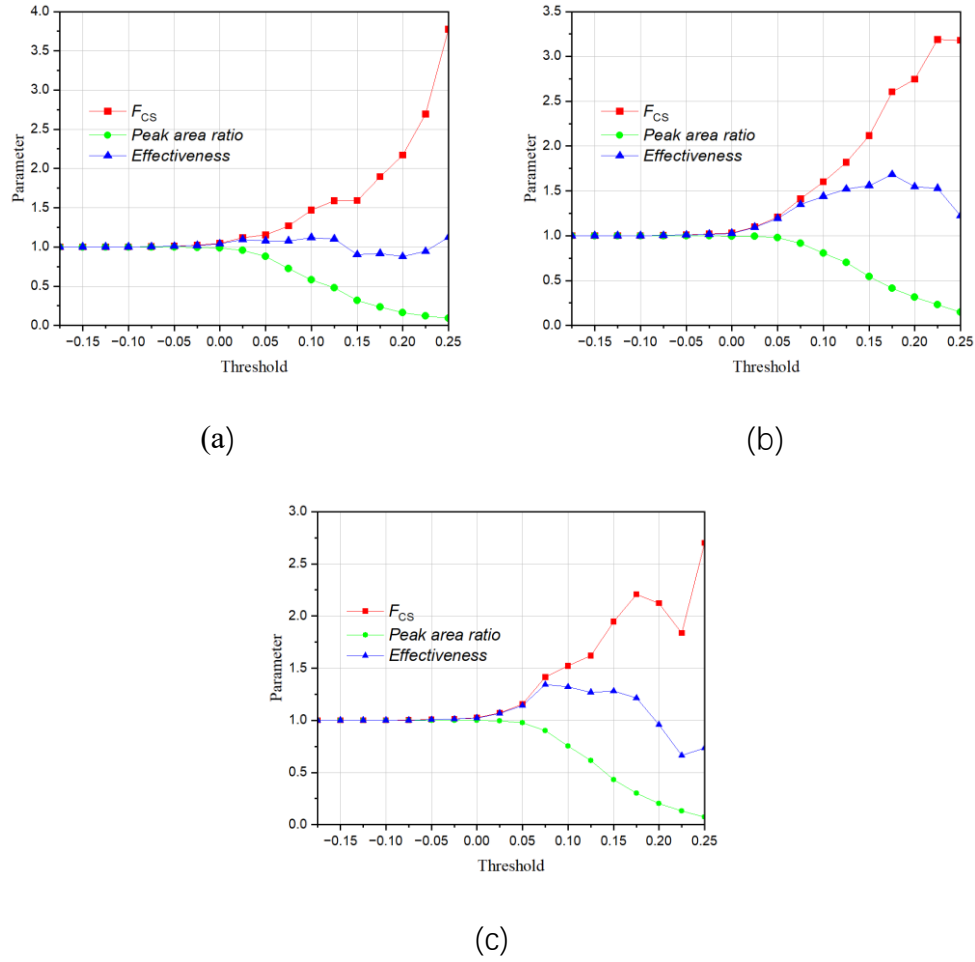


Fig. 16 Effect of the threshold value on the Compton suppression factor, peak area ratio and efficiency for deposition of the energy from (a)  $^{152}\text{Eu}$ , (b)  $^{137}\text{Cs}$  and (c)  $^{60}\text{Co}$ .

As the threshold value increases, the Compton suppression factor for the three radioactive sources rises and the peak area ratio decreases. Suppression of the Compton scattering background produces a decrease in the count over the full-energy peak range, which slows the reduction of the MDA. At a threshold value of 0.03, the Compton suppression factor can be improved while retaining the full-energy peak count to the largest possible extent. Table 4 shows the corresponding Compton suppression factor, peak area ratio and efficiency. Figure 17 shows the logarithmic energy spectrum before and after suppression of the Compton scattering background.

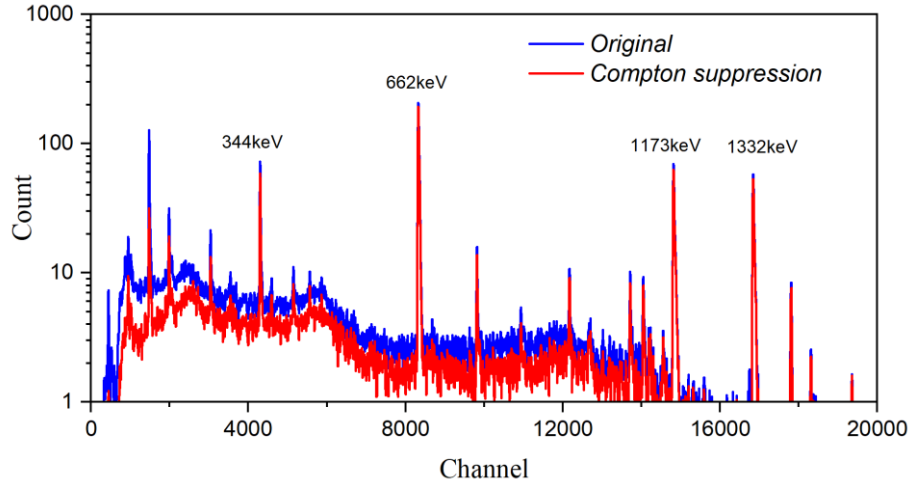


Fig. 17 Logarithmic energy spectrum before and after suppression of the Compton scattering background.

Table 4 Compton suppression factor, peak area ratio and efficiency for  $^{152}\text{Eu}$ ,  $^{137}\text{Cs}$  and  $^{60}\text{Co}$  at a threshold value of

0.03

Nuclide	Energy (keV)	Compton suppression factor	Peak area ratio	Efficiency
$^{152}\text{Eu}$	344	1.13	0.95	1.11
$^{137}\text{Cs}$	662	1.11	0.99	1.10
$^{60}\text{Co}$	1332	1.08	0.99	1.08

#### 4.6 Minimum detectable activity

The MDA is calculated using the formula given below [46-48]:

$$\text{MDA} = \frac{2.71+4.65\sqrt{B}}{m \times t \times \varepsilon \times I} \quad (26)$$

where  $B$  is the background count over the full-energy peak range,  $m$  is the sample mass,  $t$  is the measuring time,  $\varepsilon$  is the absolute detection efficiency of the respective  $\gamma$ -ray, and  $I$  is the emission intensity of the  $\gamma$ -ray.

The MDA ratio ( $a$ ) is defined as the ratio of the MDAs before and after suppression of the Compton scattering background for the same measurement. This calculation method is used to eliminate the constant in the MDA formula, thereby simplifying the calculation process. The MDA can be effectively decreased for  $a$  less than 1. The computational formula for the MDA ratio is shown below:

$$a = \frac{\text{MDA}_2}{\text{MDA}_1} = \frac{2.71+4.65\sqrt{B_2}}{2.71+4.65\sqrt{B_1}} \cdot \frac{\varepsilon_1}{\varepsilon_2} = \frac{2.71+4.65\sqrt{B_2}}{2.71+4.65\sqrt{B_1}} \cdot \frac{N_1}{N_2} \quad (27)$$

The subscripts 1 and 2 are used to denote the parameter values obtained before and after suppression of the

Compton scattering background. N denotes the count for the net peak area.

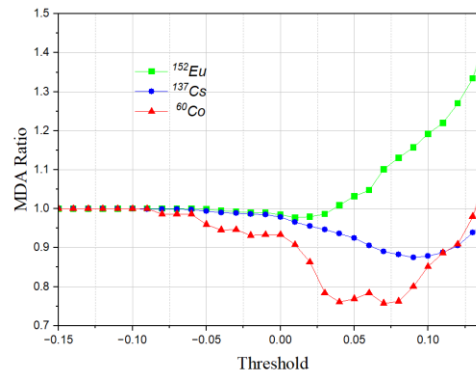


Fig. 18 Relationship between the MDA ratio and the threshold value for the three nuclides.

Table 5 shows the MDA ratio for the full-energy peak of  $\gamma$ -rays from  $^{152}\text{Eu}$ ,  $^{137}\text{Cs}$  and  $^{60}\text{Co}$  calculated using a threshold value of 0.03.

Table 5 MDA ratio for the full-energy peak of  $\gamma$ -rays from  $^{152}\text{Eu}$ ,  $^{137}\text{Cs}$  and  $^{60}\text{Co}$

Nuclide	Energy (keV)	Status	Total peak area	Net peak area	Background	Net peak area ratio	Background ratio	$a$
$^{152}\text{Eu}$	334	original	2082	1638	444	0.963	0.901	0.986
		CS	1978	1578	400			
$^{137}\text{Cs}$	662	original	8044	7760	283	0.996	0.887	0.947
		CS	7981	7730	251			
$^{60}\text{Co}$	1332	original	2740	2646	94	1.006	0.606	0.784
		CS	2718	2661	57			

Note: CS denotes Compton suppression.

According to Figure 18, using this method has resulted in a decrease in the MDA for the three energy levels of gamma rays within a certain threshold range. With the increase of gamma ray energy, the maximum reduction of MDA becomes larger in turn. Taking into consideration the optimization effect of the MDA across the entire energy range, a threshold of 0.03 is set. As shown in Table 5, at this threshold, the MDA for the full-energy peaks of gamma rays at 344 keV, 662 keV, and 1332 keV from the  $^{152}\text{Eu}$ ,  $^{137}\text{Cs}$ , and  $^{60}\text{Co}$  radioactive sources, respectively, decreased by 1.4%, 5.3%, and 21.6%.

## 5. Conclusions and Future Work

---

The proposed method can effectively suppress the Compton scattering background over the entire considered energy range. The Compton suppression factors of the radioactive sources  $^{152}\text{Eu}$ ,  $^{137}\text{Cs}$  and  $^{60}\text{Co}$  reach 1.13 (344 keV), 1.11 (662 keV) and 1.08 (1332 keV), respectively, and the corresponding MDAs decline by 1.4%, 5.3% and 21.6%. The higher the energy of the incident rays is, the larger the reduction in the MDA is. This result is obtained because the distribution of events for full-energy deposition of high-energy  $\gamma$ -rays is concentrated deep in the detector, which differs considerably from the distribution of partial-energy deposition events. Therefore, although using an ANN removes the partial-energy deposition events, more full-energy deposition events are retained than partial-energy deposition events, which reduces the count loss over the range of the full-energy peak and further decreases the MDA.

In addition to coaxial HPGe detectors, further experimental research can be conducted on systems equipped with Broad Energy Germanium (BEGe) detectors and Small Anode Germanium (SAGE) well-type detectors to extend the application range of this method.

In future studies, we will extract more decision parameters from the leading edge of pulse signals to characterize the edge shape more accurately. The accuracy of identification and classification of full- and partial-energy deposition events can be improved by increasing the number of hidden layers of the ANN model and the number of neurons in each layer, as well as by improving the activation function and training algorithm, thereby enhancing Compton suppression and decreasing the MDA.

---

## Acknowledgments

This research is supported by the National Key R&D Program of China (2022YFF0709503), the National Key R&D Program of China (2022YFB1902700), the National Key R&D Program of China (2020YFC1808304-004), National Key R&D Program of China (Grant No. 2017YFC0602101), the Key Research and Development Program of Sichuan province (Grant No. 2023YFG0347), and the Key Research and Development Program of Sichuan province (Grant No. 2020ZDZX0007).

## References

- [1] G. F. Knoll, *Radiation Detection and Measurement*, 3rd edn. (John Wiley & Sons, New York, 2000), pp. 757-774
- [2] W.H. Zhang, K. Lam, C.L. Liu, A realistic solution of overcoming disadvantage of Compton suppression spectrometer. *Appl. Radiat. Isot.* 148, 13-18 (2019). doi:10.1016/j.apradiso.2019.03.017
- [3] H.M. Badran, T. Sharshar, An experimental method for the optimization of anti-Compton spectrometer. *Nucl. Instrum. Methods Phys. Res. Sect. A-Accel. Spectrom. Dect. Assoc. Equip.* 435, 423-432 (1999). doi: 10.1016/S0168-9002(99)00573-2
- [4] W. Wahl, D. Degering, C. Lierse et al., Enhancement of Compton suppression ratios in anti-Compton techniques: the Garching and Karlsruhe photon spectrometers. *Nucl. Instrum. Methods Phys. Res. Sect. A-Accel. Spectrom. Dect. Assoc. Equip.* 369, 627-633 (1996). doi: 10.1016/S0168-9002(96)80065-9
- [5] M. TSUTSUMI, T. OISHI, N. KINOCHI et al., Design of an Anti-Compton Spectrometer for Low-Level Radioactive Wastes using Monte Carlo Techniques. *J. Nucl. Sci. Tech.* 39, 957-963 (2002). doi: 10.1080/18811248.2002.9715282
- [6] D.J.G. Love, P.J. Nolan, P.J. Smith et al., The response of a large Ge(Li)/NaI anti-compton system to evaporation neutrons. *Nucl. Instrum. Methods Phys. Res. Sect. A-Accel. Spectrom. Dect. Assoc. Equip.* 239, 639-640 (1985). doi: 10.1016/0168-9002(85)90047-6
- [7] H.M. Badran, T. Sharshar, An experimental method for the optimization of anti-Compton spectrometer. *Nucl. Instrum. Methods Phys. Res. Sect. A-Accel. Spectrom. Dect. Assoc. Equip.* 435, 423-432 (1999). doi:10.1016/S0168-9002(99)00573-2
- [8] Y. Li, W.D. Huang, S.H. Shi et al., The level structure of  $^{76}\text{Se}$  from  $^{76}\text{Br}$   $\gamma$ -decay. *Nucl. Sci. Tech.* 9, 199-208 (1998).
- [9] P. Mukherjee, P. Sen, I. Mukherjee et al., On-line neutron response of a Ge NaI(Tl) anti-compton spectrometer.

---

Nucl. Instrum. Methods Phys. Res. Sect. A-Accel. Spectrom. Dect. Assoc. Equip. 251, 191-192 (1986). doi: 10.1016/0168-9002(86)91167-8

[10] H.S. Jung, H.Y. Cho, J.H. Lee et al., Improvement of the Compton suppression ratio of a standard BGO suppressor system by a digital pulse shape analysis. Nucl. Instrum. Methods Phys. Res. Sect. A-Accel. Spectrom. Dect. Assoc. Equip. 580, 1016-1019 (2007). doi:10.1016/j.nima.2007.06.058

[11] M.G. Boulay, M. Kuźniak, Technique for surface background rejection in liquid argon dark matter detectors using layered wavelength-shifting and scintillating thin films. Nucl. Instrum. Methods Phys. Res. Sect. A-Accel. Spectrom. Dect. Assoc. Equip. 968, 163631 (2020). doi: 10.1016/j.nima.2020.163631

[12] K. von Sturm, S. Belogurov, R. Brugnera et al., A Compton scattering setup for pulse shape discrimination studies in germanium detectors. Appl. Radiat. Isot. 125, 163-168 (2017). doi: 10.1016/j.apradiso.2017.04.024

[13] Z. Zeng, Y.-H. Mi, M. Zeng et al., Characterization of a broad-energy germanium detector for its use in CJPL. Nucl. Sci. Tech. 28, 7 (2017). doi:10.1007/s41365-016-0162-y

[14] Y.H. Mi, H. Ma, Z. Zeng et al., Compton suppression in BEGe detectors by digital pulse shape analysis. Appl. Radiat. Isot. 121, 96-100 (2017). doi:10.1016/j.apradiso.2016.12.041

[15] B. Philhour, S.E. Boggs, J.H. Primbsch et al., Simulations of pulse shape discrimination (PSD) techniques for background reduction in germanium detectors. Nucl. Instrum. Methods Phys. Res. Sect. A-Accel. Spectrom. Dect. Assoc. Equip. 403, 136-150 (1998). doi: 10.1016/S0168-9002(97)01071-1

[16] RG. de Orduña, M. Hult, E. Andreotti et al., Pulse shape analysis to reduce the background of BEGe detectors. J. Radioanal. Nucl. Chem. 286, 477-482 (2010). doi: 10.1007/s10967-010-0729-8

[17] Y.-H. Mi, Z. Zeng, H. Ma et al., Improving detection sensitivity of a low background BEGe spectrometer by pulse shape discrimination using rise-time ratio. J. Radioanal. Nucl. Chem. 325, 183-189 (2020). doi:10.1007/s10967-020-07191-9

[18] Duan, Budjá, Marik et al., Pulse shape discrimination studies with a Broad-Energy Germanium detector for signal identification and background suppression in the GERDA double beta decay experiment. J. Instrum. 4, P10007 (2009). doi:10.1088/1748-0221/4/10/p10007

[19] D. Becketdahl, J. J. Blair, A. Friensehner et al., Compton rejection for HPGe detectors via real-time pulse shape analysis. Paper Presented at the 39th Annual Institute of Nuclear Materials Management Meeting, Naples, Florida, 26-30 July 1998

[20] G.J. Schmid, D. Becketdahl, J.J. Blair et al., HPGe compton suppression using pulse shape analysis. Nucl. Instrum. Methods Phys. Res. Sect. A-Accel. Spectrom. Dect. Assoc. Equip. 422, 368-372 (1998). doi:

---

10.1016/S0168-9002(98)00985-1

- [21] J.H. Lee, H.S. Jung, H.Y. Cho et al., A Novel Digital Pulse-Shape Analysis for High-Resolution Position-Sensitive Gamma-Ray Spectroscopy. *IEEE Transactions on Nuclear Science*. 57, 2631-2637 (2010). doi:10.1109/TNS.2010.2053385
- [22] J.Y. Moon, C.S. Lee, Position determination of interaction points inside a planar-type segmented germanium detector by pulse shape analysis using a three-dimensional Green's function. *Nucl. Phys. A*. 746, 643-646 (2004). doi:10.1016/j.nuclphysa.2004.09.042
- [23] H.Y. Cho, C.S. Lee, J.Y. Moon et al., Pulse shape analysis of induced charges in a segmented germanium detector by using the weighting potential method. *J. Korean Phys. Soc.* 45, 1485-1489 (2004).
- [24] M. Kurokawa, S. Shimoura, H. Iwasaki et al., Pulse shape simulation and analysis of segmented Ge detectors for position extraction. *IEEE Trans. Nucl. Sci.* 50, 1309-1316 (2003). doi:10.1109/TNS.2003.818238
- [25] I. Abt, A. Caldwell, D. Lenz et al., Pulse shape simulation for segmented true-coaxial HPGe detectors. *Eur. Phys. J. C*. 68, 609-618 (2010). doi:10.1140/epjc/s10052-010-1364-9
- [26] R.-M.-J. Li, S.-K. Liu, S.-T. Lin et al., Identification of anomalous fast bulk events in a p-type point-contact germanium detector. *Nucl. Sci. Tech.* 33, 57 (2022). doi:10.1007/s41365-022-01041-x
- [27] L.J. Harkness-Brennan, D.S. Judson, A.J. Boston et al., An experimental characterisation of a Broad Energy Germanium detector. *Nucl. Instrum. Methods Phys. Res. Sect. A-Accel. Spectrom. Dect. Assoc. Equip.* 760, 28-39 (2014). doi:10.1016/j.nima.2014.05.080
- [28] D. Barrientos, A.J. Boston, H.C. Boston et al., Characterisation of a Broad Energy Germanium (BEGe) detector. *Nucl. Instrum. Methods Phys. Res. Sect. A-Accel. Spectrom. Dect. Assoc. Equip.* 648, S228-S231 (2011). doi:10.1016/j.nima.2010.11.129
- [29] C. Unsworth, A.J. Boston, H.C. Boston et al., Characterisation of a small electrode HPGe detector. *Nucl. Instrum. Methods Phys. Res. Sect. A-Accel. Spectrom. Dect. Assoc. Equip.* 927, 293-300 (2019). doi:10.1016/j.nima.2019.02.043
- [30] M. Nakhostin, Z. Podolyak and P.J. Sellin, Application of pulse-shape discrimination to coplanar CdZnTe detectors. *Nucl. Instrum. Methods Phys. Res. Sect. A-Accel. Spectrom. Dect. Assoc. Equip.* 729, 541-545 (2013). doi:10.1016/j.nima.2013.07.073
- [31] C.-F. Yang, C.-Q. Feng, S.-B. Liu et al., FPGA-based  $\alpha/\gamma$  pulse shape discrimination for BaF<sub>2</sub> detector using 2 Gsps fast waveform sampling. *Nucl. Sci. Tech.* 28, 19 (2017). doi: 10.1007/s41365-016-0173-8
- [32] J.-L. Cai, D.-W. Li, P.-L. Wang et al., Fast pulse sampling module for real-time neutron-gamma discrimination.



---

Nucl. Sci. Tech. 30, 84 (2019). doi: 10.1007/s41365-019-0595-1

[33] J.Q. FAISAL, J.-L. Lou, Z.-H. Li et al., A pulse shape discrimination of CsI(Tl) crystal with  $^6\text{He}$  beam. Nucl. Sci. Tech. 21, 35-38 (2010). doi: 10.13538/j.1001-8042/nst.21.35-38

[34] K.-N. Li, X.-P. Zhang, Q. Gui et al., Characterization of the new scintillator  $\text{Cs}_2\text{LiYCl}_6:\text{Ce}^{3+}$ . Nucl. Sci. Tech. 29, 11 (2018). doi: 10.1007/s41365-017-0342-4

[35] I. Abt, F. Fischer, F. Hagemann et al., Simulation of semiconductor detectors in 3D with SolidStateDetectors.jl. J. Instrum. 16, P08007 (2021). doi: 10.1088/1748-0221/16/08/P08007

[36] L. Mihailescu, W. Gast, R.M. Lieder. The influence of anisotropic electron drift velocity on the signal shapes of closed-end HPGe detectors. Nucl. Instrum. Methods Phys. Res. Sect. A-Accel. Spectrom. Dect. Assoc. Equip. 447, 350-360 (2000). doi: 10.1016/S0168-9002(99)01286-3

[37] Bart Bruyneel, Peter Reiter, Gheorghe Pascovici. Characterization of large volume HPGe detectors. Part I: Electron and hole mobility parameterization. Nucl. Instrum. Methods Phys. Res. Sect. A-Accel. Spectrom. Dect. Assoc. Equip. 569, 764-773 (2006). doi: 10.1016/j.nima.2006.08.130

[38] Bart Bruyneel, Peter Reiter, Gheorghe Pascovici. Characterization of large volume HPGe detectors. Part II: Experimental results. Nucl. Instrum. Methods Phys. Res. Sect. A-Accel. Spectrom. Dect. Assoc. Equip. 569, 774-789 (2006). doi: 10.1016/j.nima.2006.08.129

[39] M. Nakhostin, *Signal Processing for Radiation Detectors*. (John Wiley & Sons, New York, 2018), pp. 6-7

[40] J. Allison, K. Amako, J. Apostolakis et al., Recent Developments in Geant4. Nucl. Instrum. Methods Phys. Res. Sect. A-Accel. Spectrom. Dect. Assoc. Equip. 835, 186-225 (2016). doi: 10.1016/j.nima.2016.06.125

[41] J. Allison, K. Amako, J. Apostolakis et al., Geant4 Developments and Applications. IEEE Trans. Nucl. Sci. 53, 270-278 (2006). doi: 10.1109/TNS.2006.869826

[42] S. Agostinelli et al., J. Allison, K. Amako et al., Geant4 - A Simulation Toolkit. Nucl. Instrum. Methods Phys. Res. Sect. A-Accel. Spectrom. Dect. Assoc. Equip. 506, 250-303 (2003). doi: 10.1016/S0168-9002(03)01368-8

[43] H.-T. Jia, S.-T. Lin, S.-K. Liu et al. High-accuracy measurement of Compton scattering in germanium for dark matter searches. Nucl. Sci. Tech. 33, 157 (2022). doi: 10.1007/s41365-022-01148-1

[44] J. Yang, Y.L. Li, Y. Tian et al., Identification of single-pixel incomplete charge collection events by using cathode waveform in pixelated CdZnTe detectors. J. Instrum. 15, P09017-P09017 (2020). doi:10.1088/1748-0221/15/09/P09017

[45] X.-C. Ming, H.-F. Zhang, R.-R. Xu et al. Nuclear mass based on the multi-task learning neural network method. Nucl. Sci. Tech. 33, 48 (2022). doi: 10.1007/s41365-022-01031-z

---

[46] G.R. Gilmore, *Practical Gamma-Ray Spectrometry*, 2nd edn. (John Wiley & Sons, New York, 2008), pp. 117-120

[47] G. Baccolo, A. Barresi, M. Beretta et al., Development of a low background alpha–beta/gamma coincidence detector. Nucl. Instrum. Methods Phys. Res. Sect. A-Accel. Spectrom. Dect. Assoc. Equip. 1003, 165290 (2021). doi: 10.1016/j.nima.2021.165290

[48] Y. Gu, K. Sun, L.-Q. Ge et al. Investigating the minimum detectable activity concentration and contributing factors in airborne gamma-ray spectrometry. Nucl. Sci. Tech. 32, 110 (2021). doi: 10.1007/s41365-021-00951-6